Adaptive-optics imaging of human cone photoreceptor distribution ◇

Toco Yuen Ping Chui, HongXin Song, and Stephen A. Burns*

School of Optometry, Indiana University, 800 E. Atwater Avenue, Bloomington, Indiana 47405, USA
**Corresponding author: staburns@indiana.edu*

Received July 29, 2008; revised October 8, 2008; accepted October 14, 2008;
posted October 15, 2008 (Doc. ID 99570); published November 19, 2008

We have used an adaptive-optics scanning laser ophthalmoscope to image the cone photoreceptor mosaic throughout the central 10°–12° of the retina for four normal subjects. We then constructed montages of the images and processed the montages to determine cone locations. Cone densities range from approximately 10,000 cones/mm^2 at 7° to 40,000 cones/mm^2 at 1°. The smallest cones were not resolved in the center of the fovea. From the locations of the cones we also analyzed the packing properties of the cone mosaic, finding that all four subjects had a slight cone streak of increased cone density and that, in agreement with previous studies using different approaches, the packing geometry decreased in regularity from the fovea toward the periphery. We also found variations in packing density between subjects and in local anisotropy across retinal locations. The complete montages are presented for download, as well as the estimated cone locations. © 2008 Optical Society of America

OCIS codes: 330.5310, 010.1080, 180.1790.

◇ **Datasets associated with this manuscript are available at** http://hdl.handle.net/10376/1088.

1. INTRODUCTION

There is evidence to suggest that the cone photoreceptor array plays a critical role in spatial sampling in the human visual system [1–4] in some regions of the retina, but not all. In the fovea, spatial sampling is limited by the optics of the eye [4–6], and, in the peripheral retina beyond approximately 10°, spatial sampling is limited by the density of ganglion cells in the retina [7–11]. Thus it is in the region from approximately 1° to 10° that cone photoreceptor packing limits spatial sampling of the environment. Since the time of Polyak [12] it has been clear that the number of cones varies dramatically across the retina over this range of eccentricities. The work of Curcio and colleagues [13–15] has given us good information on cone photoreceptor packing density and geometry across the retina. Unfortunately these data by necessity are based on histological examination of only a few eyes. Recent advances in adaptive-optics retinal imaging [16–18] now allow us to actually determine cone locations, and hence sampling, in living human eyes.

The goal of the present study is to provide the cone photoreceptor array from four emmetropic retinas from approximately 0.5° to 6° retinal eccentricity around the fovea. By using adaptive-optics scanning laser ophthalmoscope (AOSLO) imaging, we can rapidly image the retina throughout this region. However, with a single deformable mirror it is only possible to optically correct the imaging for a small region of retina at any given instant. This region is known as the isoplanatic region and is of the order of 1.5° [19]. Thus, making AOSLO imaging useful for understanding the large-scale arrangement of the human retina requires assembling a great number of individual images of adaptive-optics-corrected local regions into a large mosaic image. In the present study, we present four such mosaics, discuss how they were generated, and provide initial examples of how we systematically assessed the cone packing density at different meridians and eccentricities. We also examine local and global anisotropies in cone packing densities in the central retina of emmetropic adults. Thus, this dataset provides an initial set of normative cone data for the central 10°–12° of the retina and demonstrates the current state of our ability to compute the packing density for human eyes as a prelude to documenting disease-induced changes in the cone mosaic.

2. METHODS

A. Subjects

Four healthy emmetropes (three males and one female; age range 24–54 years, mean 37) participated in these measurements. Exclusion criteria included any retinal pathology or systemic diseases. All subjects received a complete eye examination, including a subjective refraction. Spherical equivalent refractive errors were between plano to +0.50 D (mean +0.13 D) when referenced to the spectacle plane. All subjects had best corrected visual acuity of 20/20 or better. Only the right eye was tested in this experiment. AOSLO imaging sessions for subjects 01–03 were conducted after dilating the pupils with 0.5% tropicamide, whereas subject 04 was tested without dilation. Informed consent was obtained after a full explanation of the procedures and consequences of the study. This study protocol was approved by the Indiana University Institutional Review Board and complied with the requirements of the Declaration of Helsinki.

B. Apparatus

The Indiana AOSLO system has been described in detail elsewhere [20]. For this study we used three of the primary subsystems, the wavefront sensor and deformable mirror subsystem to optimize image quality, the confocal imaging subsystem to provide high-contrast images of retinal cone photoreceptors, and the wide-field imaging subsystem to guide the imaging and provide feedback to the operator. Wavefront errors were detected with a Shack–Hartmann sensor operating at 15 Hz. The adaptive-optics control of the system was maintained through closed-loop control of a Boston Micromachines Corporation microelectromechanical systems deformable mirror via custom software. Confocal retinal images were obtained using a superluminescent diode (SLD) with a 50 nm bandwidth centered at 840 nm as a light source. Corneal power for the imaging beam was 360 μW. The imaging raster was provided by an 8 kHz horizontal scanning galvanometer and a programmable vertical scan galvanometer. For these experiments the vertical scan was programmed to provide full-frame images of 640 $\times$512 pixels at a frame rate of 15 Hz. Light returning from the retina passed through a confocal aperture optically conjugate to the retinal plane. For this study, the confocal aperture was 12 μm relative to the retina, approximately twice the size of the diffraction-limited Airy disk. The subject's head movements were stabilized using a wax impression of the mouth and a headrest. Subjects were instructed to fixate an illuminated green LED. Fixation LEDs were arranged in an 8$\times$8 array. Defocus was corrected by changing the distance between a pair of Badal lenses. Once focused and fixation was set, steering mirrors, approximately conjugated to the center of rotation of the eye, were used to position the beam sequentially across the retina with a range of 9° vertically and 10° horizontally.

C. Procedures

1. Imaging

Although imaging the operator had real-time video feedback, both from the wide-field view and high-resolution retinal images, and the Shack–Hartman wavefront sensor for pupil positioning, each displayed on a separate monitor. In each session, images were collected as short sections of video (40 frames) within a larger AVI file. Thus, for a given position of the fixation target and the displacement mirrors the operator instructed the subject to blink, waited until imaging conditions stabilized after the blink, and then initiated collection of 40 frames. The steering mirrors were then moved under experimenter control such that the new section of the retina overlapped the previous section, and the procedure was repeated. Because the range over which the steering mirrors could be moved before running into image quality problems was limited, we used five total fixation positions with rest periods between fixation positions to generate segments spanning five regions of the retina (region 1, superior temporal quadrant; region 2, inferior temporal quadrant; region 3, inferior nasal quadrant; region 4, superior nasal quadrant; and region 5, the central foveal area) [Fig. 1(a)]. Figure 1(b) shows the photoreceptor mosaics covering the entire central 12° of the retina in subject 01. The entire imaging session took approximately 1 h for each subject. The result of the imaging session was approximately 3 Gbytes of video segments. These included good frames, as well as frames that were unacceptable for some reason, either due to blinks, eye movements, or image quality, which varied rapidly, presumably due to tear-film breakup, especially toward the end of an imaging session.

2. Data Processing

The offline image processing required that we first select sets of frames that were adequate for averaging, then align and average the frames for a single retinal location, creating an averaged small field, then stitch the small field images together to create a retinal montage. Frame selection was performed using a file browser written in MATLAB (MathWorks, Inc., Natick, Massachusetts). This browser allowed the operator to step through video files, mark unacceptable frames, and view information on the hardware state and image quality (written to a database

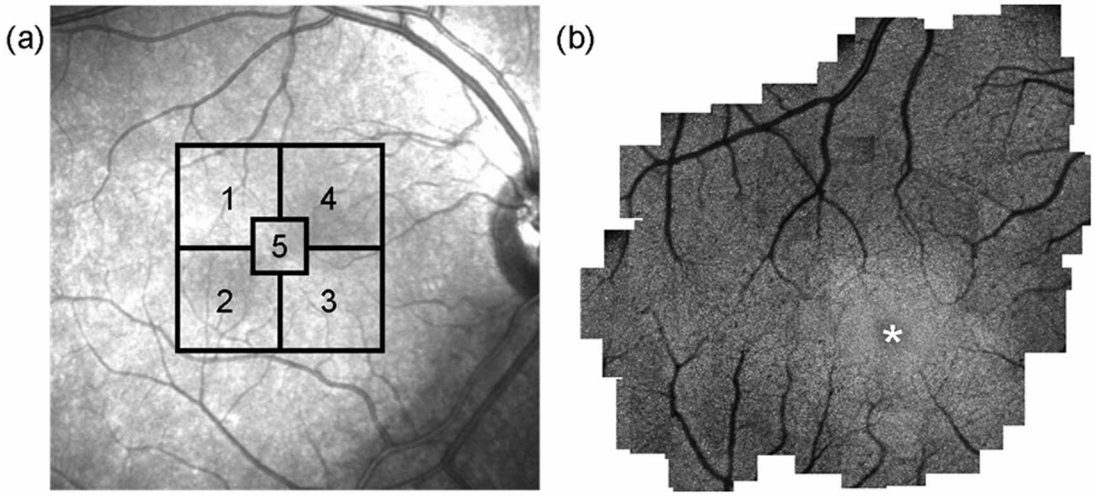

Fig. 1. (a) Retinal montages were created by imaging the cone photoreceptors in five different regions. The regions are shown schematically on a normal resolution SLO view of the retina of subject 01. (b) Montage illustrating a retinal area subtending 12°$\times$13° in subject 01. Asterisk indicates the fovea.

during image acquisition). Acceptable frames were marked for later alignment.

Image alignment was performed using a custom MATLAB program. For each local region an average was generated by choosing a template frame and then averaging successive frames to the template. The averaging was performed offline, similar to the approach based on eye movements developed by Stevenson and Roorda [21]. In our case we used small horizontal strips of retinal image, approximately 70 μm wide and 15 μm high, and found the location of the best alignment of each strip to the template. A total of 55 vertical displacements within each image were used, with successive strips overlapping the adjacent strips. We then interpolated the displacement for every line in the image and displaced them according to the template match. Images were then averaged. The number of frames contributing to an average varied from 3 to more than 30. In a few locations a single frame was used. Although averaging decreased noise and improved automatic detection of cones (described in Subsection 2.C.3), individual cones could be readily detected by eye in unaveraged frames. The variation in the number of frames averaged depended both on the subject's fixation and the overall image quality for a given subject, and in some cases the tiling of the retina was less dense than desired and eye movements would cause a region to be represented in only a few frames. The result of this step was therefore a large number of overlapping images, each approximately the size of the original video frames or slightly larger. To relate the averaged frames to each other, it was necessary to align, translate, and sometimes skew them to bring each averaged image into alignment with the others. Rotations and skews tended to be small and to occur rarely. This stage of alignment was performed manually by finding corresponding points between the selected images using Adobe Photoshop CS3 (Adobe Systems Inc., San Jose, California). A wide-field image was used to guide the operator in performing this step.

3. Determining Cone Positions

Once a complete mosaic was constructed we determined cone positions within the montage. The initial pass of this process was determined semiautomatically using a custom MATLAB program. This routine was similar to the one described by Li and Roorda [22]. To automatically determine cone locations over the full mosaic, which includes a wide range of cone spacings, we set the program to use three different filter sets, one for large cone spacing, one for medium cone spacing, and one for small cone spacing. The operator chose the filter set for individual regions of the retina. Within each filter set, all spatial parameters for the identification of the cones were adjusted as a group. For each cone size, the program first performed an unsharp mask on the cone image, removing low-spatial-frequency variations in brightness and leaving the higher frequency data, which tend to be cone photoreceptors in this type of image, but also some noise. We then performed a high-pass filter to decrease shot noise, although the averaging routine removed most of this, except in locations with only one or a few frames contributing to the final mosaic. The filtered images were then thresholded and adjusted to black-and-white images, with each white region representing a thresholded cone photoreceptor. These regions were then labeled and the locations determined. Automatic counting of cones was effective at eccentricities of >500 μm, although a manual cleanup was required to check the algorithm performance. During the recheck, local regions of the image could be reprocessed to better determine cone locations. As cone size approached the resolution limit near the fovea, automatic localization was less effective, and the degree of manual intervention required increased considerably.

4. Cone Photoreceptor Packing

Once the location of the majority of resolved cones was achieved, group properties were computed. For the current paper we concentrated on spatial variations in cone packing density, both in terms of overall contours of constant cone density and local anisotropy in cone arrangements.

Global anisotropy (sampling differences across retinal meridians) was studied by evaluating cone packing density variation between different retinal meridians in each subject. Cone packing density contour maps were generated by computing density within 22 μm $\times$ 22 μm sampling windows with 11 μm overlaps covering the entire mosaic. From these local averages a spatial map of the cone packing density was generated for each subject.

Local anisotropy (meridional variation in sampling within a local region) of the cone photoreceptor mosaic was analyzed by calculating the Fourier power spectra at 1°, 3°, 5°, and 7° retinal eccentricities along 90°, 135°, and 180° meridians. Modal Nyquist frequencies for horizontally oriented, vertically oriented, and obliquely oriented visual targets were computed from the obtained power spectra. Approximately 120 cones were included in each sampling window at different retinal eccentricities. The Fourier power spectrum for a given retinal region was discarded if a blood vessel was present within the presampled window, since this could alter the packing arrangement, either due to actual anatomical properties or due to artifactually influencing the Fourier analysis from obscuration of cones by the overlying blood vessel. Spatial autocorrelograms were also calculated at 1° and 5° for further investigation of cone packing geometry in subjects 01 and 02. Autocorrelograms were determined by sequentially putting each cone to the origin and replotting all of the relative cone positions on the same autocorrelogram [14,23].

3. RESULTS

A. Overall Montages

In general we were able to image almost the entire central 10°–12° of the retina in a single session of reasonable length for a subject. The resulting montages are shown in Fig. 2. Upon close examination of these montages it is clear that image quality varies from image segment to image segment. This occurred for several reasons. First, the system performs slightly worse when the steering mirrors are toward the edges of the Badal lenses. Presumably this is occurring because we are tapping more of the aberrations of these lenses in these positions, and the presence

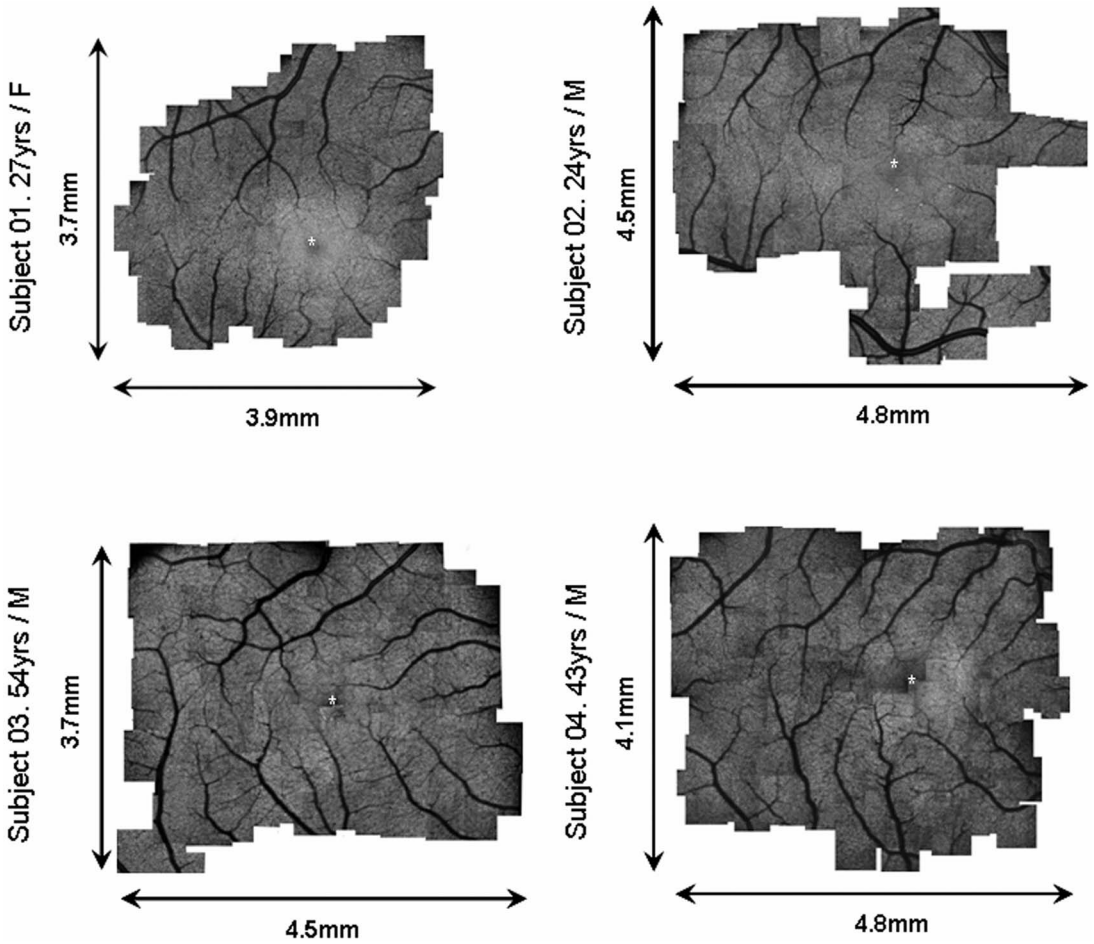

Fig. 2. Retinal montages subtending 13° to 16° retinal eccentricity from four emmetropes (View 1). Only right eyes were tested. Asterisks indicate the foveas and are present only in the PDF file, not in the high-resolution interactive views.

of nonconjugate aberrations decreases the isoplanatic area for high-quality imaging. The second, and more serious, reason is that, even within a few seconds, the optical quality of the eye is changing due to changes in the eye's tear film, and as a result, as the tear film quality decreases due to drying, the quality of even the adaptive-optics-corrected images changes, presumably because tear film aberrations can be of quite high order [24–26]. It was also apparent that head movements affected image quality. Eye position was maintained by observing the Shack–Hartmann sensor image and use of a dental mouth rest, but to keep sessions within a reasonable length for the subjects it was necessary to allow some variation from ideal position, and therefore the effective pupil size varied slightly over time as small head movements produced small pupil movements. Although the use of overlapping regions helped ensure that we obtained high image quality over most of the montage, there were regions where this was not fully successful. Even subject 04, who was tested without dilating drops, produced usable images over most of the retinal region of interest.

B. Global Anisotropy

Figure 3 shows a foveal region subtending approximately 2° in subject 01. As expected from the resolution limit of our system, individual cones could not be resolved at the center of the fovea, but all cones can be resolved at eccentricities of >200 μm (Fig. 3). As a result, from the large montages we located between 130,000 and 170,000 cones using our combined software and manual approach [Estimated locations are rounded to the nearest pixel and are available for subject 01 (Media 1), subject 02 (Media 2), subject 03 (Media 3), and subject 04 (Media 4)]. These csv data files are quite large (greater than 100,000 rows). In many systems the default program for loading csv files will be unable to open such large tables. Thus we recommend that if these data are used, the reader check that all data have been read. From these located cones, we computed cone packing density as a function of retinal eccentricity in all four montages (Fig. 4). In Fig. 4, the x and y axes represent retinal eccentricity with the origin centered at the fovea. The color bar represents the cone packing density at intervals of 5,000 cones/mm^2. Our data show that as expected, cone density decreases with increasing retinal eccentricity, it decreases from $\sim$30,000 to $\sim$15,000 cones/mm^2 from the retinal eccentricity of 500 to 1,500 μm along the temporal meridian in subject 01. Meanwhile, the cone packing density decreases from $\sim$25,000 to $\sim$10,000 cones/mm^2 from the retinal eccentricity of 500 to 1,500 μm along the superior meridian. The horizontally elongated contour lines indicate a higher cone packing density along the horizontal

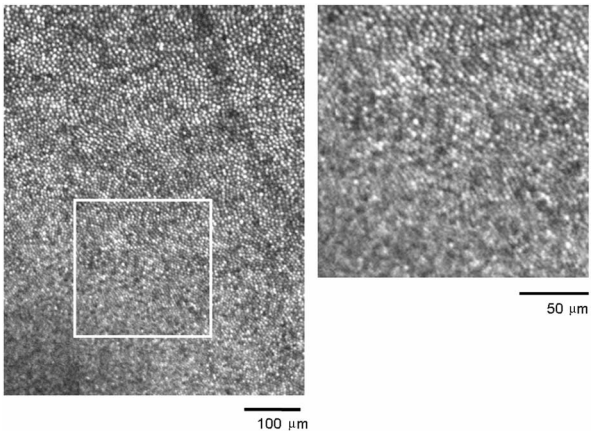

Fig. 3. Left panel, foveal image illustrating an area subtending approximately 2° in subject 01. Foveal cones are not resolved due to system resolution (2.8 μm diffraction limited). Cones from ~200 μm outward are resolved (View 2). The scale bar represents 100 μm. Right panel, magnified view of a single-frame adaptive-optics image as indicated on the left panel (View 3). The scale bar represents 50 μm.

meridian than along the vertical meridian. That is, a well-defined horizontal cone streak was observed in all subjects.

C. Local Anisotropy

Figures 5(a) and 5(b) show the sampling arrays of subject 01 at 1° and 5° retinal eccentricities at the temporal meridian. In these plots we indicate the location of approximately 120 cones within the sampling window of 56 μm $\times$ 56 μm and 108 μm $\times$ 108 μm at 1° and 5° retinal eccentricities, respectively. Spatial autocorrelograms for these regions were calculated [14,23] and the central regions are shown in Figs. 5(c) and 5(d). A distinct hexagonal cluster of points is observed in the inner ring of the autocorrelogram at 1° [Fig. 5(c)], which indicates a strong hexagonal symmetry of the cone mosaic. However, this hexagonal symmetry is no longer present at 5°, which suggests a relatively higher disorder of the cone packing in the peripheral retina [Fig. 5(d)] as has been suggested by others [5,14]. A similar autocorrelogram pattern was also observed in subject 02 and for other locations.

Local anisotropy of the cone photoreceptor mosaic was also analyzed by computing two-dimensional Fourier power spectra at 1°, 3°, 5°, and 7° retinal eccentricities along horizontal, superior, and 135° retinal meridians. Figures 5(e) and 5(f) show examples of the Fourier power spectra of the sampling arrays in Figs. 5(a) and 5(b). The distance between the origin and the peak of the ring is called the modal Nyquist frequency [27]. The nominal Nyquist frequency is half of the modal Nyquist frequency. A circular or ring-shaped appearance in the power spectrum is indicative of equal Nyquist frequency in all directions of the sampling array and would be consistent with isotropic sampling of the retinal image at this location. In practice, a perfect ring for a small sample of cones would not occur since there are variations in spacing. Nevertheless, the discrete nature of the cone images should be reflected in the Fourier transform. Thus, as was true for the autocorrelogram, Fig. 5(e) shows a relatively hexagonal shape at 1° temporal retina after Fourier transformation, suggesting the sampling array at this location is arranged in a regular fashion with hexagonal cone packing geometry. However, in Fig. 5(f), a vertically elongated ring is observed, indicating a local anisotropy at 5° temporal retina with a higher modal Nyquist frequency for horizontally oriented frequencies than for the vertically oriented frequencies.

We analyzed the variation of the potential spatial resolution of the cone sampling array by plotting the nominal Nyquist frequencies for horizontally, vertically, and obliquely (average of 45° and 135° orientation) oriented targets at different retinal eccentricities and meridians. Figure 6 shows that the nominal Nyquist frequency decreases with increasing retinal eccentricity. Nyquist frequencies in the temporal retina are the highest for horizontally oriented frequencies, followed by the obliquely and vertically oriented frequencies. Thus for the temporal meridian, the horizontal resolution is 17%–24% higher than the resolution for vertically oriented targets and 10%–14% higher than for obliquely oriented targets. In contrast, only 0%–5% difference among the Nyquist frequencies for horizontally, vertically, and obliquely oriented targets was detected at the superior meridian. Figure 7 shows that the mean of the Nyquist frequency is higher in the temporal meridian than that in the superior and 135° meridians, indicating a higher cone packing density at the temporal meridian than that in the other two meridians.

4. DISCUSSION

It is now possible to measure cone locations and packing geometry over most of the central retina and to do so in a relatively rapid manner. By keeping imaging sessions to approximately an hour, we can characterize the cone array from approximately 1° to approximately 9° retinal eccentricity. These data allow researchers to start to analyze the spatial properties of the retinal sampling array. The results obtained are in general agreement with the relatively sparse information from careful histological studies of fresh human retina [15]. More detailed analyses are clearly possible, and we present these montages for others to use.

A. Cone Sampling Array

To investigate the transformation of visual information from the outside world to high-level perception and cognition, it is necessary to understand the transfer of information through the visual system. In the past, standard models of optics and retinal sampling were used to understand what information was available. In recent years the development of rapid and accurate wavefront sensing [20,28–30] has allowed us to understand the large role of individual differences in retinal image quality between individuals. Now with the development of adaptive-optics imaging of the cone mosaic [16–18,20], we can also understand the nature of the sampling of the natural world by the photoreceptor matrix. One thing that is clear from the mosaics presented, as well as other data [15,31–33], is that there are large individual differences in the spatial sampling imposed by the photoreceptor matrix. For instance, in our data, subject 02 has relatively higher cone

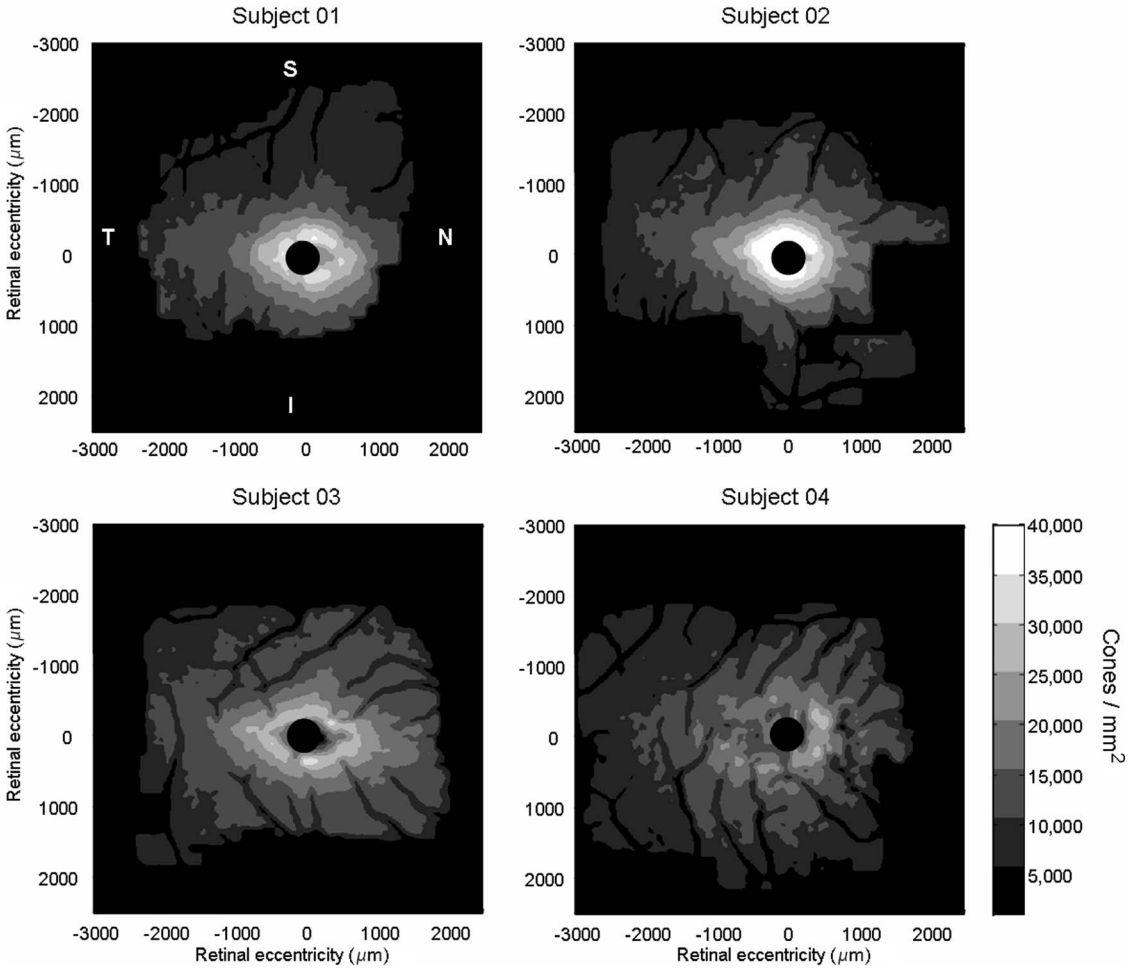

Fig. 4. Cone density contours for four emmetropes (View 4). The x and y axes represent retinal eccentricity with the origin centered at the fovea. Cone density estimates within the central 500 μm have been removed due to the resolution limit of our system. The color bar indicates cone density at intervals of 5,000 cones/mm^2. Upper left, cone density contour map of subject 01 (Media 1) (S, superior retina; I, inferior retina; T, temporal retina; N, nasal retina). In this subject, cone density decreases from ~30,000 to ~15,000 cones/mm^2 from the retinal eccentricity of 500 to 1,500 μm along the temporal meridian. Meanwhile, cone packing density decreases from ~25,000 to ~10,000 cones/mm^2 from the retinal eccentricity of 500 to 1,500 μm along the superior meridian. The horizontally elongated contour lines indicate a higher cone density along the horizontal meridian. Other panels, cone density contour maps for subjects 02–04 (Media 2, Media 3, Media 4), as indicated.

densities at the retinal eccentricity from ~200 to ~500 μm than subjects 03 and 04, but lower cone packing densities in the peripheral retina. Ultimately, models of human vision will be able to better understand the complexities of central processing if they include data on constraints that spatial filtering by the optics and photoreceptor sampling place on the visibility of the natural world. As an example, the natural world tends to have a $1/f$ spatial frequency spectrum; however, by the time this external frequency spectrum is first filtered by the optical system and then sampled by a spatially varying sampling pattern, the spectrum available to central processes is quite different.

B. Global Anisotropy

The cone packing density data for the emmetropic eyes are in reasonable agreement with the data reported by Curcio *et al.* [15] for postmortem measurements. The cone packing density contour maps shown in Fig. 4 reveal a minor global anisotropy that is stable across eccentricity with the highest cone density at the horizontal meridian. Curcio *et al.* reported cone density for human retina decreases from 37,000 to 15,000 cones/mm^2 from the retinal eccentricity of 500 to 1500 μm at the temporal meridian, whereas our data show that cone density decreases from 30,000 to 15,000 cones/mm^2 across the same retinal eccentricity. Similarly, their data indicated that cone density decreases from 28,000 to 13,000 cones/mm^2 from the retinal eccentricity of 500 to 1500 μm at the superior meridian, whereas our data show a reduction from 25,000 to 10,000 cones/mm^2 across the same retinal eccentricity. These results are consistent with a previous report of the cone streak in the human retina [15], but we did find a difference between cone densities near the fovea. In fact, previous experiments have also reported a considerable variation in foveal cone density between individuals [15,32–34]. In addition, no obvious nasotemporal asymmetry in cone packing density is observed within the central retina of 5 mm, which is also evident in other anatomical studies [14,15].

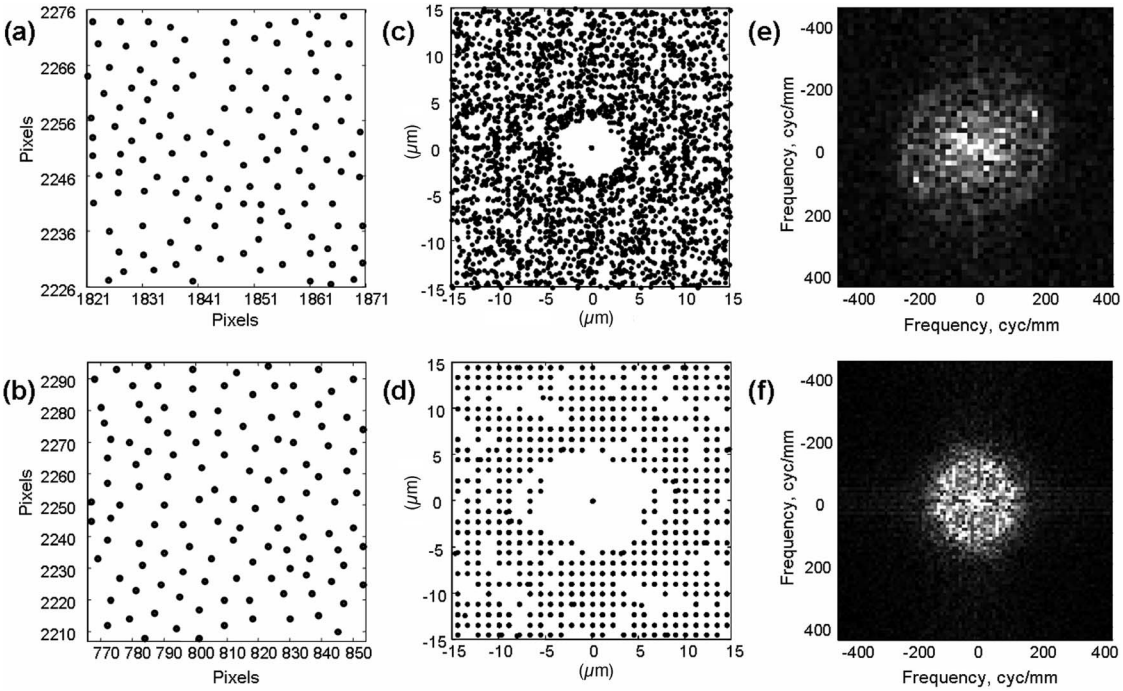

Fig. 5. Change in sampling properties with retinal position for subject 01. First row, 1° retinal eccentricity; second row, 5° eccentricity. Panels (a) and (b) show the sampling arrays of subject 01 at 1° and 5° retinal eccentricities at the temporal meridian. (c) and (d) show the spatial autocorrelograms of the corresponding sampling arrays in (a) and (b), respectively. (c) A distinct hexagonal cluster of points indicates a hexagonal arrangement of cones in the spatial autocorrelogram at 1°. (d) This hexagonal symmetry no longer exists at 5°, which suggests a disorder of the cone packing of the peripheral retina. (e) A relatively hexagonal shape at 1° temporal retina after Fourier transformation, suggesting the sampling array is arranged in a regular fashion with hexagonal cone packing geometry. (f) A vertically elongated ring is observed, indicating a local anisotropy at 5° temporal retina with a higher modal Nyquist frequency for a horizontally oriented target than for vertically oriented frequencies.

C. Local Anisotropy

Throughout the perifoveal and parafoveal retinal regions, our *in vivo* imaging reveals local anisotropy similar to that reported for a single cadaver eye [14]. The classic study by Curcio and Sloan had suggested that the most regular cone packing area is located at 0.7°–1.2° retinal eccentricity. Other studies have also shown hexagonal arrangement of cone photoreceptors in the primate fovea [12,14,35,36]. Our *in vivo* findings [Fig. 5(c)] are in agreement with these anatomical studies with hexagonal packing geometry at 1° temporal retina, but not at 5°. Curcio and Sloan also reported anisotropic variations in the cone sampling at different positions in the retina. Near the fovea they found an axial ratio in the autocorrelogram of 1.02–1.10, comparable with our measurement of a 1.10 axial ratio at 1° retinal eccentricity. Further from the fovea the sampling increases in its anisotropy. Thus, the present study supports that the human cone photoreceptors are arranged hexagonally near the fovea with the degree of regularity decreasing as the retinal eccentricity increases [5,14], perhaps due to rod intrusion into the photoreceptor sampling array beginning at the eccentric-

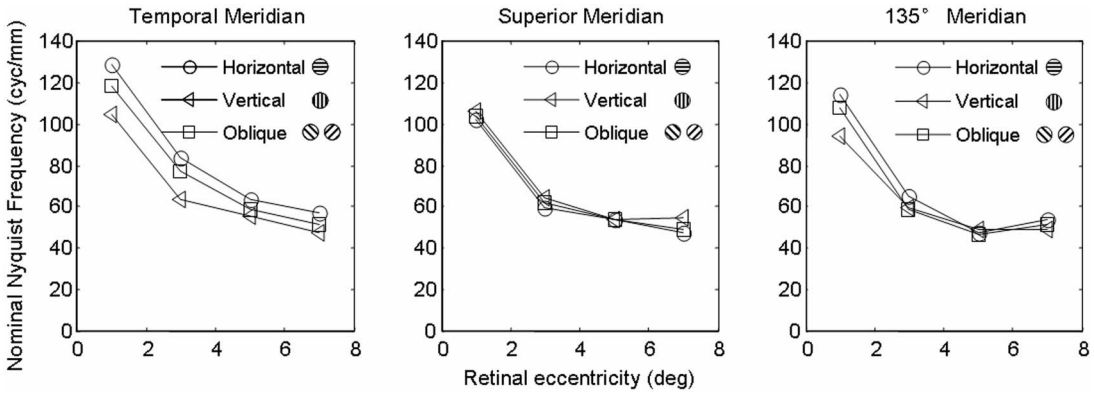

Fig. 6. Nominal Nyquist frequency as a function of retinal eccentricity at temporal (left panel), superior (middle panel), and 135° (right panel) meridians. Nyquist frequencies for horizontally, vertically, and obliquely oriented targets were computed from the Fourier power spectra at different retinal eccentricities and meridians. The Nyquist frequency at the temporal retina is the highest in the horizontally oriented frequencies, followed by the obliquely and vertically oriented frequencies. The difference is less obvious in the superior and 135° meridians.

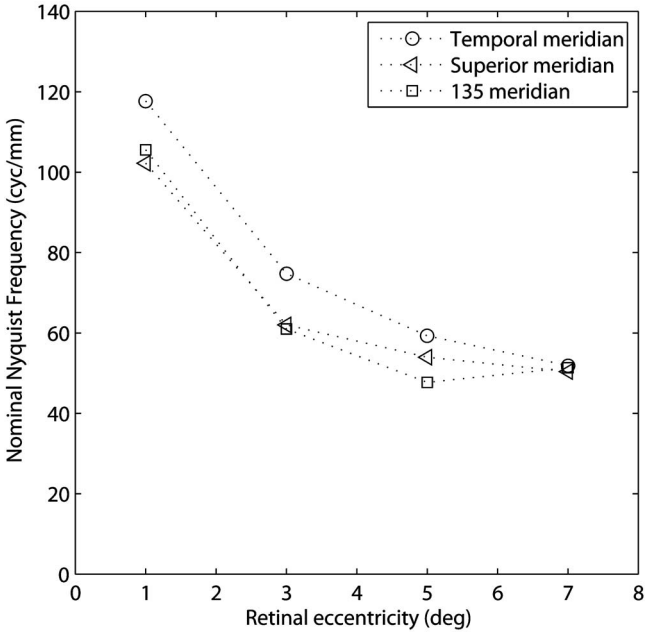

Fig. 7. Mean of the nominal Nyquist frequency as a function of retinal eccentricity at the temporal, superior, and 135° meridians. The mean Nyquist frequency is higher in the temporal meridian than that in the superior and 135° meridians, indicating a higher cone packing density at the temporal meridian than that in the other two meridians

ity of 0.7° [5].

Figure 6 shows the dependence of the nominal Nyquist frequencies for differently oriented targets along different meridians. We find that the nominal Nyquist frequency is 17%–24% and 10%–14% higher for a horizontally oriented target than for vertically and obliquely oriented targets along the temporal meridian, respectively. These results also support the idea of a systematic local anisotropy with cone spacing smaller in the vertical direction than in the horizontal direction on the retina. This effect is smaller for differently oriented targets in the superior and 135° meridians, suggesting a relatively isotropic cone packing geometry along these meridians. Curcio and Sloan found slightly smaller anisotropies, 10%–15%, with the highest spacing parallel to the meridian being measured. That is, they found a radial anisotropy as well as a cone streak, but with smaller differences than we report for a single eye [14]. Williams, using a psychophysical method on four observers found a cone spacing 14% greater along the horizontal meridian than along the vertical meridian for measurements within 1.75° of the fovea [5].

The calculated nominal Nyquist frequency at three retinal meridians is shown as a function of retinal eccentricity in Fig. 6. Our finding of Nyquist frequencies at 1°–7° temporal retina decreasing from 117 cyc/mm (34 cyc/deg) to 52 cyc/mm (15 cyc/deg) are in agreement with prior psychophysical studies of resolution acuity along the horizontal meridian [9,37]. This match has been taken as evidence that resolution acuity is limited by cone packing density within 10° eccentricity. Although our findings are in agreement with previous psychophysical studies for resolution acuity, it should be noted that they are not consistent with the psychophysical oblique effect for the central visual field [37–39]. The oblique effect states that visual performance is better for horizontal and vertical than for obliquely oriented targets [40]. It has been suggested that the origin of this local anisotropy is due to a postreceptoral mechanism rather than optical or retinal sampling factors [41,42] and the present results would reinforce that conclusion, since the sampling array cannot explain it. Also shown in Fig. 7 are the mean nominal Nyquist frequencies for three meridians. These data are consistent with prior anatomical [15] and psychophysical [43] studies of higher cone packing density and visual acuity along the horizontal meridian.

5. CONCLUSIONS

Throughout the retina, *in vivo* imaging reveals global and local anisotropies similar to those reported for postmortem measurements and that are also consistent with psychophysical measurements of higher visual acuity along the horizontal meridian. The main contribution of the present study is to demonstrate that it is now possible to systematically obtain measurements of human cone photoreceptor sampling properties over much of the parafovea of the human retina *in vivo* in a single imaging session. This will allow us not only to better understand the normal retina, but also to understand how other factors such as aging and retinal disease affect the cone photoreceptors both globally and locally for individual subjects. By measuring the locations of more than 100,000 cones in a single imaging session, adaptive-optics imaging holds the promise of avoiding sampling biases when examining the retina at high resolution. Clearly, data processing and information extraction on the resulting data sets needs to be improved, and we hope that by providing these large mosaics, they can act not only as a reference for further experiments in detecting and monitoring retinal diseases, but also as a seed for better algorithm development and to start the process of building a database of individual variations in the human retina.

ACKNOWLEDGMENTS

The authors thank Arthur Bradley and Larry Thibos for their helpful discussions. This work was supported by National Institutes of Health (NIH) grants R01-EY14375 and R01-EY04395.

REFERENCES

1. D. R. Williams, "Seeing through the photoreceptor mosaic," Trends Neurosci. **9**, 193–198 (1986).
2. D. R. Williams and R. Collier, "Consequences of spatial sampling by a human photoreceptor mosaic," Science **221**, 385–387 (1983).
3. J. Hirsch and C. A. Curcio, "The spatial resolution capacity of human fovea," Vision Res. **29**, 1095–1101 (1989).
4. D. R. Williams and N. J. Coletta, "Cone spacing and the visual resolution limit," J. Opt. Soc. Am. A **4**, 1514–1523 (1987).
5. D. R. Williams, "Aliasing in human foveal vision," Vision Res. **25**, 195–205 (1985).
6. F. W. Campbell and D. G. Green, "Optical and retinal factors affecting visual resolution," J. Physiol. (London) **181**, 576–593 (1965).
7. S. J. Anderson and R. F. Hess, "Post-receptoral

undersampling in normal human peripheral-vision," Vision Res. **30**, 1507–1515 (1990).
8. L. N. Thibos, D. L. Still, and A. Bradley, "Characterization of spatial aliasing and contrast sensitivity in peripheral vision," Vision Res. **36**, 249–258 (1996).
9. L. N. Thibos, F. E. Cheney, and D. J. Walsh, "Retinal limits to the detection and resolution of gratings," J. Opt. Soc. Am. A **4**, 1524–1529 (1987).
10. N. J. Coletta and T. Watson, "Effect of myopia on visual acuity measured with laser interference fringes," Vision Res. **46**, 636–651 (2006).
11. S. J. Anderson, K. T. Mullen, and R. F. Hess, "Human peripheral spatial resolution for achromatic and chromatic stimuli: limits imposed by optical and retinal factors," J. Physiol. (London) **442**, 47–64 (1991).
12. S. L. Polyak, *The Retina* (U. Chicago Press, 1941).
13. C. A. Curcio, K. R. Sloan, Jr., O. Packer, A. E. Hendrickson, and R. E. Kalina, "Distribution of cones in human and monkey retina: individual variability and radial asymmetry," Science **236**, 579–582 (1987).
14. C. A. Curcio and K. R. Sloan, "Packing geometry of human cone photoreceptors: variation with eccentricity and evidence for local anistropy," Vision Res. **9**, 169–180 (1992).
15. C. A. Curcio, K. R. Sloan, R. E. Kalina, and A. E. Hendrickson, "Human photoreceptor topography," J. Comp. Neurol. **292**, 497–523 (1990).
16. J. Liang, D. R. Williams, and D. T. Miller, "Supernormal vision and high-resolution retinal imaging through adaptive optics," J. Opt. Soc. Am. A **14**, 2884–2892 (1997).
17. A. Roorda, "Adaptive optics ophthalmoscopy," J. Refract. Surg. **16**, S602–S607 (2000).
18. A. Roorda, F. Romero-Borja, W. J. Donnelly, H. Queener, T. J. Hebert, and M. C. W. Campbell, "Adaptive optics scanning laser ophthalmoscopy," Opt. Express **10**, 405–412 (2002).
19. P. Bedggood, M. Daaboul, R. Ashman, G. Smith, and A. Metha, "Characteristics of the human isoplanatic patch and implications for adaptive optics retinal imaging," J. Biomed. Opt. **13**, 024008 (2008).
20. S. A. Burns, R. Tumbar, A. E. Elsner, D. Ferguson, and D. X. Hammer, "Large-field-of-view, modular, stabilized, adaptive-optics-based scanning laser ophthalmoscope," J. Opt. Soc. Am. A **24**, 1313–1326 (2007).
21. S. B. Stevenson and A. Roorda, "Correcting for miniature eye movements in high resolution scanning laser ophthalmoscopy," Proc. SPIE **5288**, 145–151 (2005).
22. K. Y. Li and A. Roorda, "Automated identification of cone photoreceptors in adaptive optics retinal images," J. Opt. Soc. Am. A **24**, 1358–1363 (2007).
23. D. H. Wojtas, B. Wu, P. K. Ahnelt, P. J. Bones, and R. P. Millane, "Automated analysis of differential interference contrast microscopy images of the foveal cone mosaic," J. Opt. Soc. Am. A **25**, 1181–1189 (2008).
24. R. Montes-Mico, A. Caliz, and J. L. Alio, "Wavefront analysis of higher order aberrations in dry eye patients," J. Refract. Surg. **20**, 243–247 (2004).
25. S. Koh, N. Maeda, T. Kuroda, Y. Hori, H. Watanabe, T. Fujikado, Y. Tano, Y. Hirohara, and T. Mihashi, "Effect of tear film break-up on higher-order aberrations measured with wavefront sensor," Am. J. Ophthalmol. **134**, 115–117 (2002).
26. S. Koh and N. Maeda, "Wavefront sensing and the dynamics of tear film," Cornea **26**, S41–S45 (2007).
27. N. J. Coletta and D. R. Williams, "Psychophysical estimation of extrafoveal cone spacing," J. Opt. Soc. Am. A **4**, 1503–1513 (1987).
28. J. Liang, B. Grimm, S. Goetz, and J. F. Bille, "Objective measurements of wave aberrations of the human eye with the use of a Hartmann–Shack wave-front sensor.," J. Opt. Soc. Am. A **11**, 1949–1957 (1994).
29. L. N. Thibos, X. Hong, A. Bradley, and R. A. Applegate, "Accuracy and precision of objective refraction from wavefront aberrations," J. Vision **4**, 329–351 (2004).
30. R. Navarro, "Measurement, modeling and improvement of optical image quality in human eyes," Acta Phys. Pol. A **101**, 147–158 (2002).
31. T. Y. Chui, H. Song, and S. A. Burns, "Individual variations in human cone photoreceptor packing density: variations with refractive error," Invest. Ophthalmol. Visual Sci. **49**, 4679–4687 (2008).
32. P. K. Ahnelt, H. Kolb, and R. Pflug, "Identification of a subtype of cone photoreceptor, likely to be blue sensitive, in the human retina," J. Comp. Neurol. **255**, 18–34 (1987).
33. C. Yuodelis and A. Hendrickson, "A qualitative and quantitative analysis of the human fovea during development," Vision Res. **26**, 847–855 (1986).
34. G. A. Osterberg, "Topography of the layer of rods and cones in the human retina," Acta Ophthalmol. **13 Suppl 6**, 1–97 (1935).
35. J. Hirsch and R. Hylton, "Quality of the primate photoreceptor lattice and limits of spatial vision," Vision Res. **24**, 347–356 (1984).
36. J. I. Yellott, "Spectral consequences of photoreceptor sampling in the rhesus retina," Science **221**, 382–385 (1983).
37. J. Rovamo, V. Virsu, P. Laurinen, and L. Hyvarinen, "Resolution of gratings oriented along and across meridians in peripheral vision," Invest. Ophthalmol. Visual Sci. **23**, 666–670 (1982).
38. M. A. Berkley, F. Kitterle, and D. W. Watkins, "Grating visibility as a function of orientation and retinal eccentricity," Vision Res. **15**, 239–244 (1975).
39. F. W. Campbell, J. J. Kulikowski, and J. Levinson, "The effect of orientation on the visual resolution of gratings," J. Physiol. (London) **187**, 427–436 (1966).
40. S. Appelle, "Perception and discrimination as a function of stimulus orientation: the 'oblique effect' in man and animals," Psychol. Bull. **78**, 266–278 (1972).
41. L. Maffei and F. W. Campbell, "Neurophysiological localization of the vertical and horizontal visual coordinates in man," Science **167**, 386–387 (1970).
42. F. W. Campbell and J. J. Kulikowski, "Orientational selectivity of the human visual system," J. Physiol. (London) **187**, 437–445 (1966).
43. R. S. Anderson, M. O. Wilkinson, and L. N. Thibos, "Psychophysical localization of the human visual streak," Optom. Vision Sci. **69**, 171–174 (1992).